Electromagnetic Science
vol. 1, no. 3, 0030202, September 2023
https://doi.org/10.23919/emsci.2023.0020

Research Article

Low-Cost Beam Steering that Covers the Entire Azimuthal Plane Powered by Amplitude-Only Synthesis of a Quintuple-Dipole Source

Da Yi[1,2], Zhiyang Qi[1,2], Mingchun Tang[1,2], Dajiang Li[1,2], Yilin Lang[1,2], and Xingchang Wei[3]

1. *The Key Laboratory of Dependable Service Computing in Cyber Physical Society Ministry of Education, College of Microelectronics and Communication Engineering, Chongqing University, Chongqing 400044, China*
2. *Chongqing Key Laboratory of Space Information Network and Intelligent Information Fusion, Chongqing University, Chongqing 400044, China*
3. *College of Information Science and Electronic Engineering, Zhejiang University, Hangzhou 310027, China*

Corresponding author: Mingchun Tang, Email: tangmingchun@cqu.edu.cn.
Received May 31, 2023; Accepted July 20, 2023; Published Online August 15, 2023.

Abstract — A new amplitude-only synthesis approach in quintuple electric dipoles (EDs) is proposed to enable the regulation of power flow in the azimuthal plane. The regulation methodology is investigated analytically with double ED, triple ED and quintuple ED models. First, when the phase difference between the EDs switches, the double ED model, acting as a reconfigurable source, can work in two modes with different power flow directions, i.e., unidirectional mode and bidirectional mode. Then, from the triple ED model, it is verified that the power flow in the two working modes can be regulated to the desired direction in the azimuthal plane with high precision by controlling the feeding amplitudes of the dipoles. Moreover, a quintuple ED model is developed to enhance the symmetry and consistency of the power flow regulation in the plane. Finally, a prototype of the azimuthal beam steering system, including digitally controlled radio-frequency (RF) frontend tuning circuits, optimized practical feeding elements, and an end-fire radiator, is designed, fabricated and measured. Both unidirectional and bidirectional modes are observed, and satisfactory single-beam and dual-beam steering performance in the azimuthal plane is achieved. Unlike most phased arrays that realize beam steering by configuring phases, the beam steering of the proposed reconfigurable source in each mode can be arbitrarily synthesized only by the amplitudes of the quintuple feeding elements, which provides a new route for realizing low-cost and multifunctional beam-steering systems.

Keywords — Electric dipole, Reconfigurable devices, Amplitude-only synthesis, Beam steering.
Citation — Da Yi, Zhiyang Qi, Mingchun Tang, *et al.*, "Low-Cost Beam Steering that Covers the Entire Azimuthal Plane Powered by Amplitude-Only Synthesis of a Quintuple-Dipole Source," *Electromagnetic Science*, vol. 1, no. 3, article no. 0030202, 2023. doi: 10.23919/emsci.2023.0020.

I. Introduction

With the rapid development of fifth-generation (5G) communication and the Internet of things (IoT), there is an increasing demand for miniaturized, multistate, and high-performance beam steering devices. Limited by the inherent relationship between the size of analog circuits/antennas and their working performance, such as bandwidth and efficiency, it is very challenging to integrate a large number of circuits and antennas into a highly constrained space to construct ultracompact, high-performance and multistate beam steering devices. To address this challenging problem, the reconfigurable approach, where the structures designed in a shared space are reconfigured to guide the power flow into different spatial regions for different beam steering states, has become one of the most attractive solutions. For RF frontend applications, the current existing reconfigurable methods for controlling power flow can be generally divided into the following three categories.

The first category is the use of analog or digital switches in the current flowing pathways in the circuits and antennas [1]–[10], where the switches are embedded in circuits or radiative metallic structures to select the desired working section. Therefore, their ON/OFF states can determine the temporal functionality of the circuits and antennas.

The second category is to employ novel active metasurfaces [11]–[22]. Different from the first category, these metasurfaces are arranged in the incident direction of propagating waves, and the spatial incident waves will be absorbed, scattered or transmitted by the metasurfaces with a certain amplitude and phase differences according to the

configured states of the metasurface; thus, the amplitude of the power that flows in different azimuth angles can be efficiently controlled. Within this category, except for employing a number of conventional switches [11]–[17], many other materials, such as phase-changing materials [18], [19], liquid crystals [20], and graphene [21], [22], are utilized for the manipulation of spatial waves.

The third category adopts active sources [23]–[38]. Phased array antennas can achieve beam steering by configuring the amplitudes and phases of the feeding ports [23]–[25]. Moreover, in recent years, the combination of electric dipoles (EDs) and magnetic dipoles (MDs) has been widely studied for generating unidirectional beams, e.g., Huygens source antennas [7], [8], [26]–[30], Huygens source-based waveguide power dividers [31], and the excitation sources for controlling unidirectional propagation due to the spin-momentum locking phenomenon in different waveguides [32]–[37]. It has been demonstrated in these studies that the phase difference between EDs and MDs can determine the direction of power flow. Some works further increase the number of dipoles and RF feeding components to construct a Huygens box [38] to realize desired wavefronts in a closed region by controlling the amplitudes and phases of these dipoles.

Although these approaches have been validated theoretically or experimentally, they still face the following crucial problems in regulating the power flow. To increase the working states in the first two design approaches, a large number of switches, tunable materials, and bias structures should be utilized, which would result in problems of increased complexity, large insertion loss, low space utilization and high cost. For the third approach, the phased array antennas and the Huygens box require a large number of phase and amplitude controlling RF circuits, which make the cost relatively high. Moreover, the reported Huygens source antennas, waveguide dividers, and sources for exciting near-field spin-momentum locking phenomena only realize power flow regulation in two opposite directions or very limited azimuth regulation states. Note that, as a hot research topic in recent years, MIMO systems [39]–[42] have been increasingly used for beam steering. In addition to the above power flow regulation methods, digital beamforming is attracting increasing attention. However, digital beamforming is realized by many processes, such as algorithm processing, modulation and demodulation, which will lead to a larger time delay and a larger insertion loss. Consequently, for the regulation of power flow in the azimuthal plane, it is still challenging to realize multiple steering states with low delay, complexity, loss, and cost.

In this paper, we propose a new reconfigurable source to eliminate the above stated problems, where the source is constructed by quintuple EDs. The reconfigurable source has two working modes, i.e., unidirectional mode and bidirectional mode. Interestingly, under the two working modes, the power flow can be arbitrarily regulated to the desired angles in four quadrants of an azimuthal plane, only by controlling the amplitudes of the dipoles, which differs from the approach of controlling directivity by configuring the port phases in conventional phased array antennas and the approach of controlling the radiation pattern by utilizing multiple switches in reconfigurable antennas. Based on this amplitude-only synthesis technique, a prototype of the azimuthal beam steering system is designed, fabricated and validated. In each working mode, it can realize 360° unidirectional/bidirectional beam steering in the azimuthal plane by employing only three RF amplitude tuning circuits and two switches, which paves the way for miniaturized, low-cost, and high-performance multibeam steering systems for various applications.

This paper is arranged as follows. In Section II, the analytical field analysis of double, triple and quintuple EDs is successively implemented to interpret the working mechanism of the reconfigurable source, and the reconfigurable source is designed with electric feeding elements (EFEs) in the plane-plate waveguide (PPW) scenario as a preliminary validation of the reconfigurable source. In Section III, the azimuthal beam steering system is proposed based on the optimized reconfigurable source in PPW. Its prototype was optimized, fabricated and tested. The measured results are in good agreement with the simulated results, which demonstrates that the system can realize the steering of unidirectional beams and bidirectional beams in the entire azimuthal plane. Finally, some conclusions are drawn in section VI.

II. Proposed Reconfigurable Source

1. Operating mechanism

The conceptual evolution of the proposed reconfigurable source is shown in Figure 1. The three ideal models, i.e., double, triple and quintuple ED models, are proposed to illustrate the working mechanism.

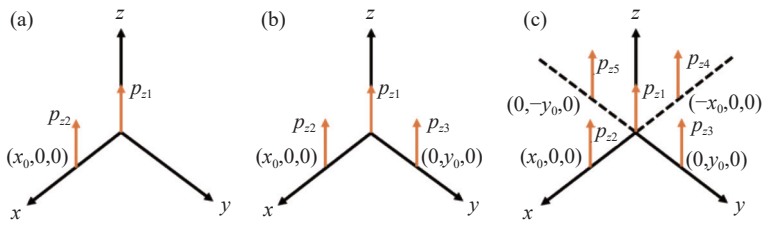

Figure 1 Configuration of the (a) Double ED model, (b) Triple ED model, and (c) Quintuple ED model.

1) Double EDs model

The double ED model, as shown in Figrue 1(a), consists of two EDs, i.e., $p_{z1} = A_1 e^{j\varphi_1}$ located at the original point and $p_{z2} = A_2 e^{j\varphi_2}$ at (x_0, 0, 0), in which A_1 and A_2 and φ_1 and φ_2 are the amplitudes and phases of p_{z1} and p_{z2}, respectively. The amplitudes have units of Ampere · meter (A·m). The far-field electric fields radiated by the two EDs are derived as [43]

$$E_1 = j\omega\mu A_1 e^{j\varphi_1} \frac{e^{-jkr}}{4\pi r} \sin\theta\hat{\theta} \tag{1}$$

$$E_2 = j\omega\mu A_2 e^{j\varphi_2} \frac{e^{-jkr}}{4\pi r} e^{jkx_0 \sin\theta\cos\phi} \sin\theta\hat{\theta} \tag{2}$$

where ω is the radian frequency, μ is the permeability in the vacuum, r is the distance from the reconfigurable source to an observation point in the far field, and k is the wavenumber. Thus, the total electric field is

$$E_{\text{total}} = j\omega\mu \frac{e^{-jkr}}{4\pi r} \sin\theta\hat{\theta}\left(A_1 e^{j\varphi_1} + A_2 e^{j\varphi_2} e^{jkx_0 \sin\theta\cos\phi}\right) \tag{3}$$

The field distribution in the azimuthal plane $\theta = 90°$ is analyzed. If the two EDs have the same amplitude, $A_1 = A_2$, and their phases satisfy

$$\Delta\varphi_x = \varphi_2 - \varphi_1 = \pi - kx_0 \cos\phi_0 \tag{4}$$

the total field would be zero in the $\phi = \pm\phi_0$ direction in the plane, considering that the cosine function is an even function. From the above equation, one can introduce the magnitude-nulls in the radiated electric field. Here, assuming $x_0 = 5$ mm, the total electric field at 10 GHz in the $\theta = 90°$ plane is calculated when $\Delta\varphi_x$ varies, as shown in Figure 2. It is noted that equation (4) can be satisfied only when $\Delta\varphi_x$ is within the range $[\pi - kx_0, \pi + kx_0]$, i.e., [120°, 240°]. Therefore, only the cases of $\Delta\varphi_x$ in this range are presented. Specifically, it can be seen that when $\Delta\varphi_x$ = 120° or 240°, the electric field will be canceled in the direction ϕ = 0° or 180° and enhanced in the opposite direction, which exhibits unidirectional radiation performance.

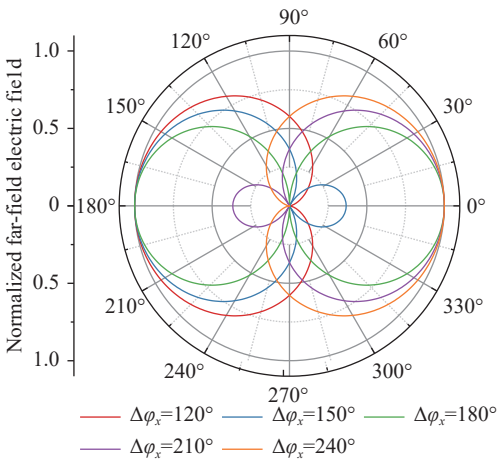

Figure 2 The normalized electric field of the double ED model when $\Delta\varphi_x$ varies.

Moreover, when $\Delta\varphi_x$ = 180°, the electric field will be canceled in the lines ϕ = 90° and 270° and has dual beams pointing toward ϕ = 0° and 180°, which exhibits bidirectional radiation performance. Since the far-field power is proportional to the square of the electric field, the power flow is controlled. The above phenomenon indicates that two active EDs can operate in unidirectional and bidirectional modes to generate single-beam and dual-beam radiation.

Here, two issues should be mentioned. On the one hand, for the unidirectional mode, its performance is similar to that of the Yagi-Uda antenna [9], [44], [45]. However, since the EDs are active in our framework, there are no passive parasitic elements, such as reflectors and directors, and the distance between the active EDs could be smaller than the spacing between the reflector and the director required in the typical Yagi-Uda antenna [38], which is approximately λ/4 to λ/2, because the phase difference introduced by the feeding ports can compensate for the decrement of the phase resulting from the distance. For example, in the proposed example shown in Figure 2, x_0 = 5 mm is only λ/6 at 10 GHz. On the other hand, the proposed method can also be applied for the near-field case, but the condition will be different from (4). To focus on amplitude-only beam steering, we only consider the far-field case for brevity.

2) Triple EDs model

On the basis of the above analysis, we further study the triple ED model for the regulation of the power flow direction in an azimuthal plane. Compared with the double ED model, the triple ED model introduces an additional ED, i.e., $p_{z3} = A_3 e^{j\varphi_3}$ located at (0, y_0, 0). It is easy to derive the total electric field radiated by the three EDs, which is presented as (5) at the bottom of this page. Here, we assume $y_0 = x_0 = 5$ mm and $\varphi_3 = \varphi_2$, i.e., $\Delta\varphi_y = \varphi_3 - \varphi_1 = \varphi_2 - \varphi_1 = \Delta\varphi_x$, and then from the conclusion of the double ED model, it can be deduced that when the amplitude combination switches from $A_2 = A_1$, $A_3 = 0$ to $A_3 = A_1$, $A_2 = 0$, in both unidirectional and bidirectional modes, the reconfigurable source will radiate toward the direction ϕ = 0°/270° and ϕ = 90°/180°, respectively. Therefore, it is reasonable that if we configure the amplitude combination with $A_2 \neq 0$ and $A_3 \neq 0$, the transition states, where the power flows toward other angles in the four quadrants, would be observed. To realize a good power balance between the three EDs to achieve field cancellation and enhancement at certain angles, the amplitudes of the three EDs are set based on the following condition:

$$A_1 = \sqrt{A_2^2 + A_3^2} \tag{5}$$

Then, we fix A_1 to 2 A·m and make A_2 vary within [0, A_1] to calculate the normalized electric field in the azimuthal plane θ = 90°, as shown in Fig. 3. For the unidirec-

tional mode ($\Delta\varphi_x$ = 120° or 240°) presented in Figure 3(a) and (b), when A_2 increases, the direction of the maximum power flow is gradually regulated from ϕ = 0° to ϕ = 90° or from ϕ = 180° to ϕ = 270°. For the bidirectional mode ($\Delta\varphi_x = \pi$) presented in Figure 3(c), the direction of the maximum power flow is gradually regulated from ϕ = 0° & 180° to ϕ = 90° & 270°. For the regulation of the two working modes in the first quadrant, i.e., the cases of Figure 3(a) and (c), the regulated direction can be approximately characterized as

$$\phi = \arctan(A_3/A_2) \tag{6}$$

which indicates that the direction can be arbitrarily controlled if the feeding amplitudes have high resolution. Here, we highlight that the directivity is controlled by feeding amplitudes under fixed feeding phases, which is distinct from conventional planar phased-array antennas [23]. The above numerical results verify the efficacy of utilizing different amplitude combinations of the EDs to regulate the power flow in an azimuthal plane.

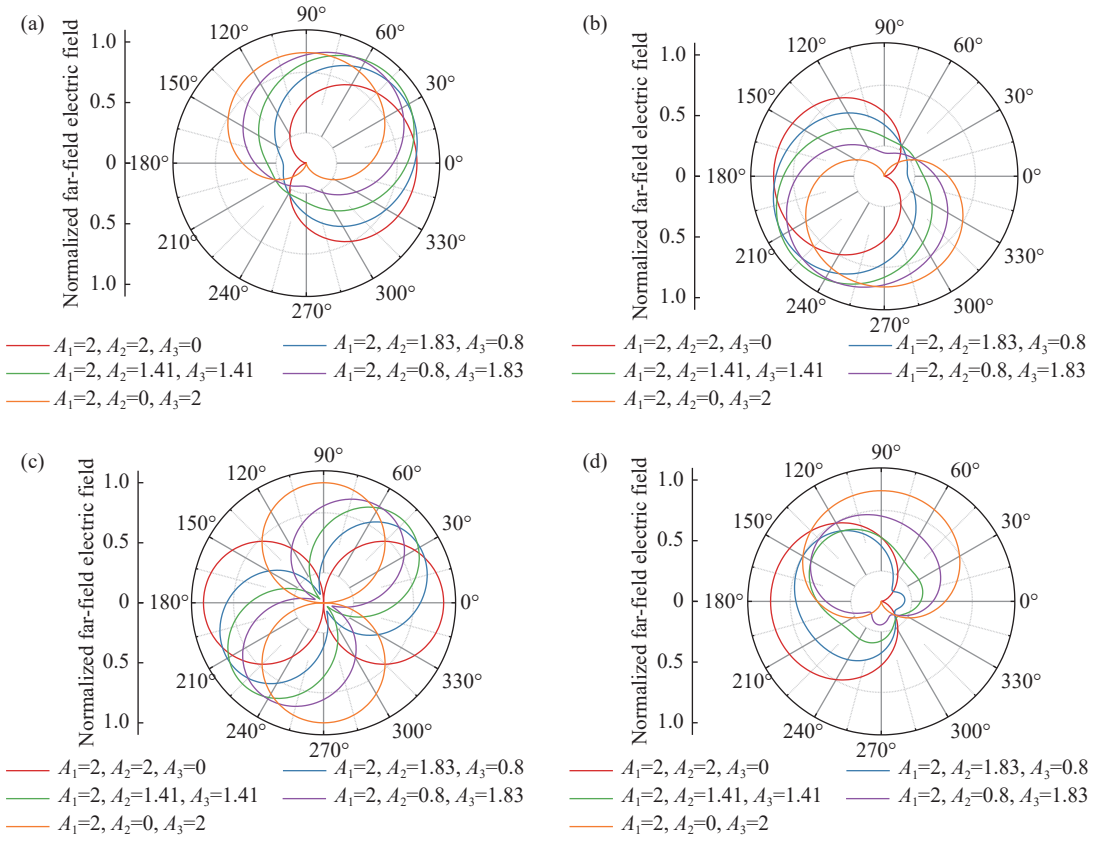

Figure 3 The normalized azimuthal far-field electric field of the triple ED model under different feeding amplitude combinations when (a) $\Delta\varphi_x = \Delta\varphi_y$ = 240°, (b) $\Delta\varphi_x = \Delta\varphi_y$ = 120°, (c) $\Delta\varphi_x = \Delta\varphi_y$ = 180°, and (d) $\Delta\varphi_x$ = 120, $\Delta\varphi_y$ = 240°.

Note that for the triple ED model, there are two existing problems. First, the regulation range is limited in the first and third quadrants. Second, in the regulation process of the unidirectional mode, the front-to-end ratio of the power flow deteriorates in the transition states, which can be seen in Figure 3(a) and (b). For the former problem, one may infer that if $\Delta\varphi_x \neq \Delta\varphi_y$, the power flow direction could be regulated in the second and fourth quadrants. Here, an example is proposed for investigation in detail. We assume $\Delta\varphi_x$ = 120° and $\Delta\varphi_x$ = 240°. It is easy to deduce that when the amplitude combination switches from $A_2 = A_1$, A_3 = 0 to $A_3 = A_1$, A_2 = 0, the power flow direction changes from ϕ = 180° to ϕ = 90°, which indicates that the transition states of the two amplitude combinations may result in the regulation of power flow in the second quadrant. Following the condition of (6), we present the results of the transition states in Figure 3(d). Although the direction can be regulated, the pattern of the radiated electric field suffers from an unacceptable distortion due to the asymmetric phase of p_{z2} and p_{z3}.

3) Quintuple EDs model

To further address these intrinsic problems in the triple ED model, the quintuple ED model shown in Figure 1(c) is proposed, where two additional EDs, i.e., p_{z4} and p_{z5}, are introduced and arranged on the -x and -y axes. In such a framework, on the one hand, to regulate the power flow in a certain quadrant, proper EDs can be selected and combined to obtain the optimum performance. Since the four EDs surrounding the center one (p_{z1}) are symmetrically located, the

regulation in the four quadrants would have better consistency. Similar to (7), when the deflection angle is determined, the relationship between the excitation amplitudes is represented as (11). On the other hand, when three EDs are selected to regulate power flow in a certain quadrant, such as the cases shown in Figure 3(a), the left two EDs could be properly fed to cancel the backward power flow to improve the directivity of the power flow.

$$E_{\text{total}} = \mathrm{j}\omega\mu\frac{\mathrm{e}^{-\mathrm{j}kr}}{4\pi r}\sin\theta\hat{\theta}\left(A_1\mathrm{e}^{\mathrm{j}\varphi_1} + A_2\mathrm{e}^{\mathrm{j}\varphi_2}\mathrm{e}^{\mathrm{j}kx_0\sin\theta\cos\phi} + A_3\mathrm{e}^{\mathrm{j}\varphi_3}\mathrm{e}^{\mathrm{j}ky_0\sin\theta\sin\phi}\right) \tag{7}$$

$$E_{\text{total}} = \mathrm{j}\omega\mu\frac{\mathrm{e}^{-\mathrm{j}kr}}{4\pi r}\sin\theta\hat{\theta}\left(A_1\mathrm{e}^{\mathrm{j}\varphi_1} + A_2\mathrm{e}^{\mathrm{j}\varphi_2}\mathrm{e}^{\mathrm{j}kx_0\sin\theta\cos\phi} + A_3\mathrm{e}^{\mathrm{j}\varphi_3}\mathrm{e}^{\mathrm{j}ky_0\sin\theta\sin\phi} + A_4\mathrm{e}^{\mathrm{j}\varphi_4}\mathrm{e}^{-\mathrm{j}kx_0\sin\theta\cos\phi} + A_5\mathrm{e}^{\mathrm{j}\varphi_5}\mathrm{e}^{-\mathrm{j}ky_0\sin\theta\sin\phi}\right) \tag{8}$$

$$E_{\text{total}} = \mathrm{j}\omega\mu\frac{\mathrm{e}^{-\mathrm{j}kr}}{4\pi r}\hat{\theta}\left[\alpha_c A_{E1}\mathrm{e}^{\mathrm{j}\varphi_{E1}} + \alpha_s\left(A_{E2}\mathrm{e}^{\mathrm{j}\varphi_{E2}}\mathrm{e}^{\mathrm{j}kx_0\cos\phi} + A_{E3}\mathrm{e}^{\mathrm{j}\varphi_{E3}}\mathrm{e}^{\mathrm{j}ky_0\sin\phi}\right)\right] \tag{9}$$

$$E_{\text{total}} = \mathrm{j}\omega\mu\frac{\mathrm{e}^{-\mathrm{j}kr}}{4\pi r}\hat{\theta}\left[\alpha_c A_{E1}\mathrm{e}^{\mathrm{j}\varphi_{E1}} + \alpha_s\left(A_{E2}\mathrm{e}^{\mathrm{j}\varphi_{E2}}\mathrm{e}^{\mathrm{j}kx_0\cos\phi} + A_{E3}\mathrm{e}^{\mathrm{j}\varphi_{E3}}\mathrm{e}^{\mathrm{j}ky_0\sin\phi} + A_{E4}\mathrm{e}^{\mathrm{j}\varphi_{E4}}\mathrm{e}^{-\mathrm{j}kx_0\cos\phi} + A_{E5}\mathrm{e}^{\mathrm{j}\varphi_{E5}}\mathrm{e}^{-\mathrm{j}ky_0\sin\phi}\right)\right] \tag{10}$$

$$\phi = \begin{cases} \arctan(A_2/A_3) & \text{(Quadrant 1)} \\ \pi/2 + \arctan(A_3/A_4) & \text{(Quadrant 2)} \\ \pi + \arctan(A_4/A_5) & \text{(Quadrant 3)} \\ 3\pi/2 + \arctan(A_5/A_2) & \text{(Quadrant 4)} \end{cases} \tag{11}$$

To validate the above proposed method, numerical calculation is implemented according to the derived total electric field of the quintuple EDs model shown as (8). Here, we first study the effectiveness of the directivity improvement technique based on additional EDs. The case of the power flow pointing to ϕ = 45° is utilized for study. Figure 4(a) shows that, as predicted, when A4 and A5 increase from 0 to 0.5 A·m, the front-to-back ratio increases from 3.5 to 13.7 (from 10.88 dB to 22.72 dB). Then, we fix the feeding amplitude of the two additional EDs to 0.3 A·m and calculate the radiation patterns of the quintuple ED model under different feeding amplitude configurations according to (11), as shown in Figure 4(b). It can be seen that the power flow direction could be arbitrarily regulated in the azimuthal plane with a good front-to-back ratio, and the pattern consistency in different quadrants is highly improved compared with those in Figure 3(a) and (d). Therefore, the quintuple ED model highly improves the performance of the triple model and is undoubtedly more suitable for the practical application of the reconfigurable source.

2. Preliminary design in PPW

After discussing the working mechanism of the reconfigurable source in free space, we design a practical reconfigurable source in the PPW scenario for verification. This design is not only a preliminary structural realization of the ideal reconfigurable source but also a preparation for the integration of RF frontend controlling circuits and the radiation source because the metal planes in PPW can serve as the shielding ground between the complex circuits and radiators to avoid serious interference. The configurations of

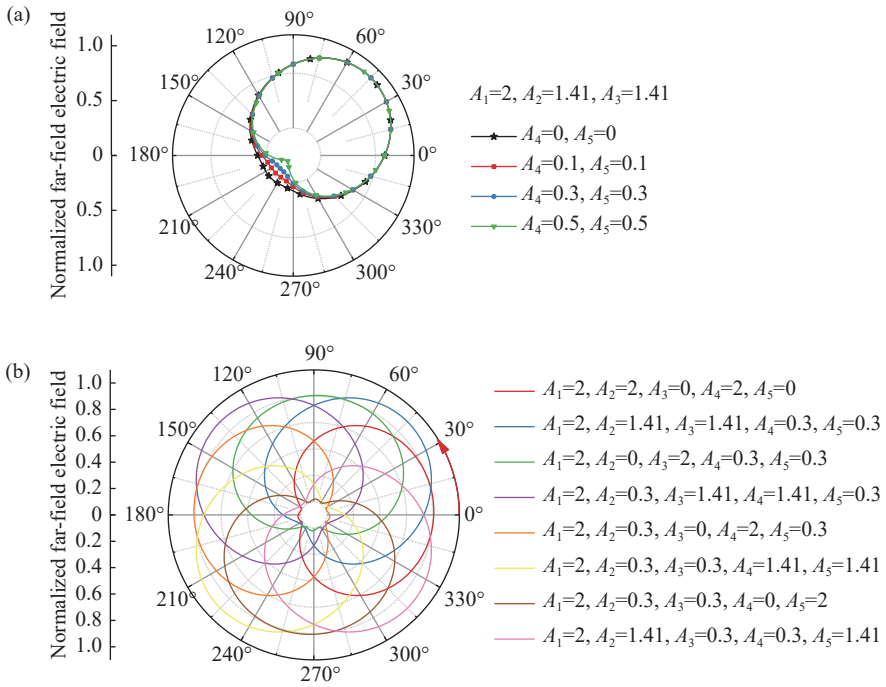

Figure 4 The normalized far-field electric field of the quintuple ED model in the azimuth plane when (a) A_4 and A_5 vary under a fixed scanning angle and (b) different feeding amplitudes are applied for the unidirectional working mode.

the two designed reconfigurable sources in the PPW, which are constructed by three and five electric feeding elements (EFEs) for comparison, are shown in Figure 5(a) and (b). The EFEs are cylindrical monopoles, which can be equivalent to electric dipoles [31]. The PPW is constructed by upper and bottom perfect electric conductor (PEC) disks. The side face surrounding the PPW is set as the radiation boundary for conveniently observing the power flow regulation behavior. For the quintuple EFE model, one EFE is placed in the center of the PPW, while the other four EFEs are located at the $\pm x$ and $\pm y$ axes, with a distance of 5 mm to the central EFE. The five EFEs are fed with coaxial waveports for numerical study. The constructive parameters in this model are shown in Table 1. For the triple EFE model, compared with the quintuple model, although two EFEs are removed, the other configuration is the same.

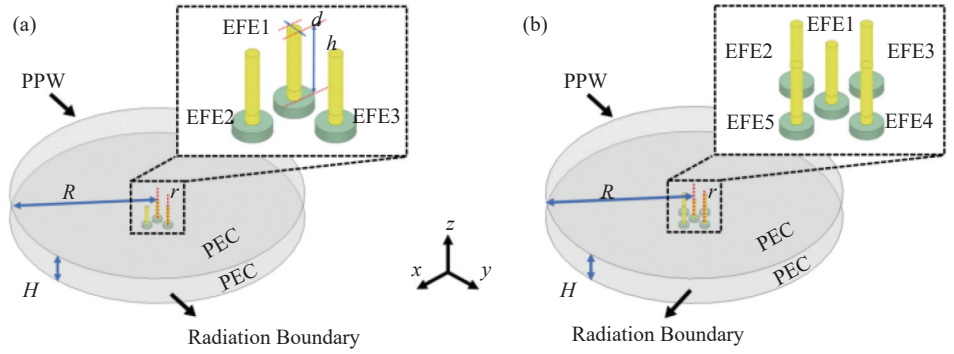

Figure 5 The design of the proposed reconfigurable source in the PPW. (a) Triple EFEs model; (b) Quintuple EFEs model.

Table 1 Physical dimensions of the EFEs in the PPW (unit: mm)

R	r	H	d	h
50	5	10.16	1.24	6

The simulated reflection coefficients of the three EFEs and five EFEs in the PPW are shown in Figure 6(a) and (b). Because the EFEs are not perfectly matched, equations (5) and (8) should be modified as equations (9) and (10), in which A_{En} and φ_{En} (n = 1 to 5) are the amplitudes and phases of the nth EFE, $\alpha_c = |\alpha_c|e^{j\Delta c}$ and $\alpha_s = |\alpha_s|e^{j\Delta s}$ are the modification factors of the feeding amplitudes and phases, considering the difference between the practical feeding structures in the PPW and the ideal dipoles in free space and the reflection of the ports. Note that in the PPW scenario, because the power is constrained between two PEC surfaces, the term $\sin(\theta)$ in the electric field of the EFEs is set to $\sin(90°)$ in (9) and (10). Since the two equations have the same forms as (5) and (8), the power flow regulation in the PPW follows the same rule proposed in Section II.1.

In the PPW scenario, to ensure that the electric fields radiated by the EFEs have a good amplitude balance, taking the triple EFEs model as an example, the condition that is similar to (6) should be satisfied, which is

$$|\alpha_c|A_{E1} = \sqrt{|\alpha_s A_{E2}|^2 + |\alpha_s A_{E3}|^2} \tag{12}$$

To achieve the above condition, the incident powers of the three waveports should be set to satisfy the following equation:

$$P_{E1}\left(1-|R_{E1}|^2\right) = P_{E2}\left(1-|R_{E2}|^2\right) + P_{E3}\left(1-|R_{E3}|^2\right) \tag{13}$$

in which P_{En} and R_{En} are the magnitude of the incident power and the reflection coefficient at the three waveports.

In addition to the amplitude balance consideration, it should be noted that the phase shifts on the EFEs, which are introduced by the practical feeding structures, should be considered. They can be obtained by comparing the electric field distributions generated by the EFEs with those gener-

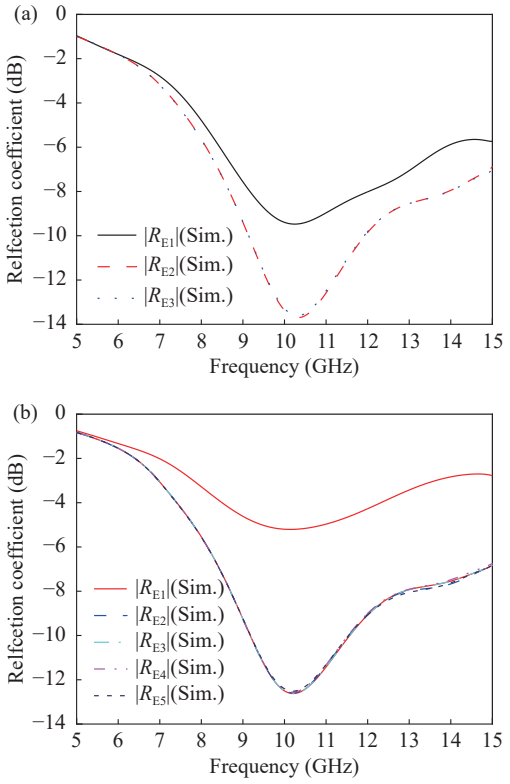

Figure 6 Simulated reflection coefficients for EFEs in the (a) triple and (b) quintuple ED models.

ated by the ideal dipoles. Here, we take the unidirectional mode working in the first quadrant as an example. For the triple EFE model, it is found that the central EFE and the surrounding EFEs bring phase shifts of $\Delta_c = -5°$ and $\Delta_s = 70°$, while for the quintuple EFE model, $\Delta_c = -30°$ and $\Delta_s = -85°$. Therefore, the actual phase of the signals fed into the PPW by the EFE and MFEs should be $\varphi'_{E1} = \varphi_{E1} + \Delta_c$ and $\varphi'_{Ei} = \varphi_{Ei} + \Delta_s$ (i = 2 to 5).

According to (13) and the extracted phase shifts introduced by the practical EFEs, several combinations of the amplitudes of the EFEs are configured to validate the working performance. For the unidirectional mode of the triple EFE model, the regulation of the power flow in the first quadrant is shown in Figure 7(a). Due to the asymmetric arrangement of the EFEs, when P_{E2} or P_{E3} = 0, the radiation pattern does not exactly point to ϕ = 90° or ϕ = 0°. Moreover, when the radiation pattern points to ϕ = 45°, the front-to-back ratio decreases to ~8 dB.

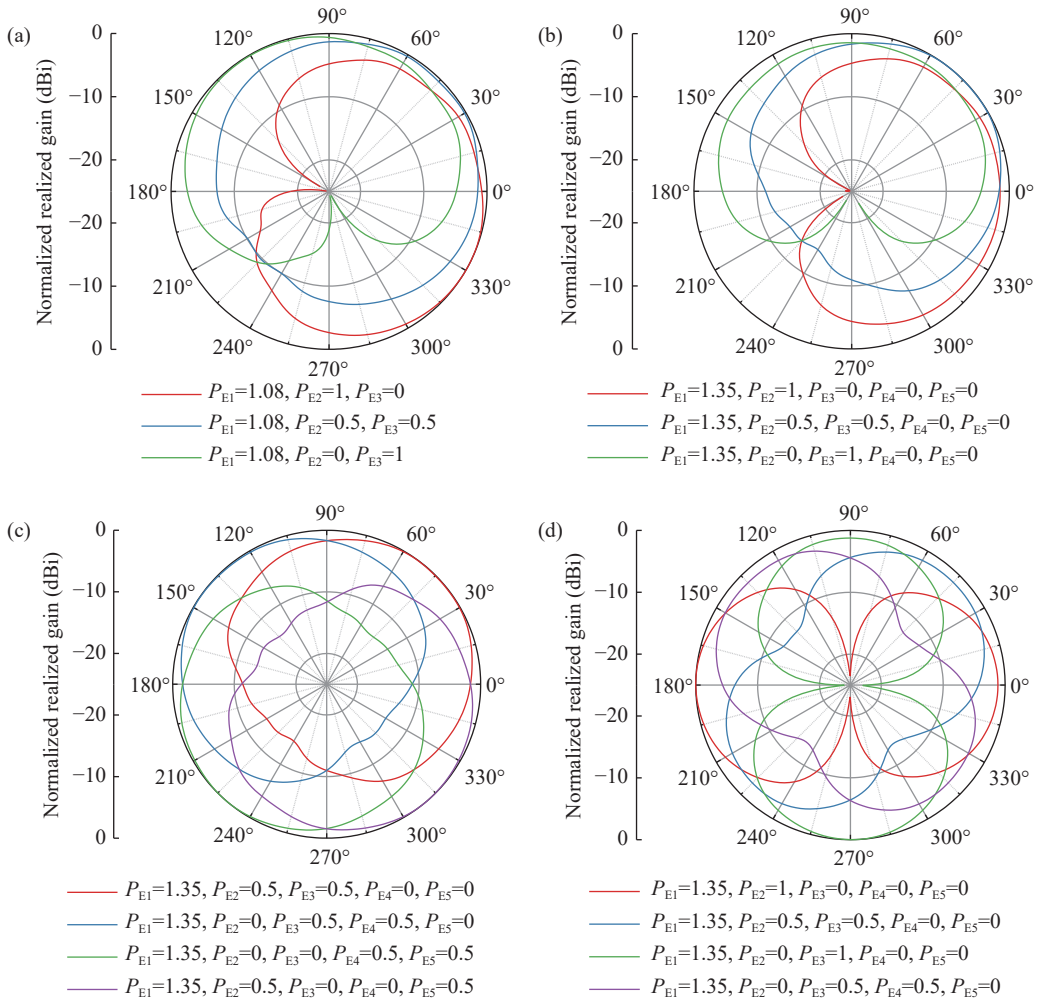

Figure 7 The normalized radiation patterns of (a) the triple EFE model in the first quadrant under the unidirectional mode and the quintuple EFE Model (b) in the first quadrant under the unidirectional mode, (c) in the four quadrants under the unidirectional mode, and (d) in the four quadrants under the bidirectional mode.

In contrast, the unidirectional radiation patterns of the quintuple EFE model in the same quadrant are shown in Figure 7(b). The symmetry of the patterns is significantly improved, and the front-to-back ratio in all states is larger than 13 dB, which validates the effectiveness of the two additional EFEs. It should be mentioned that the feeding amplitude of the two additional EFEs is set to 0 in the quintuple EFE model. Different from directly feeding the two EFEs with a small amplitude as that in the ideal cases in Figure 4, here, the scattering of the practical structure of the two additional EFEs can equivalently serve as two radiation sources with a small feeding amplitude to compensate for the backward radiation and increase the directivity. In the above design, two switches can be introduced to select the combination of waveport 2 / waveport 4 and waveport 3 / waveport 5 to achieve power flow regulation in the four quadrants. Therefore, for this design, in each working mode, only three methods of amplitude controlling circuits and two switches are required to realize the arbitrary regulation of power flow in the horizonal plane, which can maximally lower the design complexity and cost. Finally, we also presented the regulation performance of the quintuple

EFE model in the four quadrants under both the unidirectional and bidirectional modes, as shown in Figure 7(c) and Figure 7(d), where good radiation pattern consistency and symmetry are realized, and the radiation nulls are all 10 dB smaller than the peak realized gain. Note that to further enhance the directivity, the above quintuple EFE model can be employed as a subarray to extend the scale of the antenna array.

III. Azimuthal Beam Steering System Based on a Reconfigurable Source

Based on the working mechanism and the practical feeding elements introduced in the previous section, we develop an azimuthal beam steering system to demonstrate the practical application of the reconfigurable source, as shown in Figure 8. The system is composed of a circular patch, a ground plane, five EFEs, and RF front-end circuits. The circular patch is printed on the upper face of an FR4 substrate, which has a relative dielectric constant $\varepsilon_r = 4.4$, loss tangent tan $\delta = 0.02$, and thickness of 1 mm. The ground plane is made of a copper plate with a thickness of 1 mm. The circular patch and ground plane form a PPW with a thickness of 8 mm, and the power from the reconfigurable source will propagate to the edge of this PPW and radiate through the aperture between the patch and ground plane. We notice that the impedance matching of the central EFE would deteriorate to above −6 dB when it is surrounded by four similar EFEs, as shown in Figure 6(b). Therefore, we propose the structure of the EFEs as shown in Figure 8(d) and (e), where the central EFE adopts the planar inverted trapezoidal structure, and the surrounding EFEs employ the ellipse strip loaded monopole to obtain a good impedance matching performance within the same frequency range. From Figure 8(f), we can see that the current on the EFE has an even-symmetry distribution and dominant ±*z*-direction components, which is similar to that of the monopole. In addition, Figure 8(g) shows its electric field distribution in the PPW, which is the typical omnidirectional distribution radiated by the monopole. Therefore, the ellipse strip is similar to the monopole antenna and can be further equivalent to the electric dipole analyzed in the theory section. All feeding elements are printed on Rogers 4350 substrates

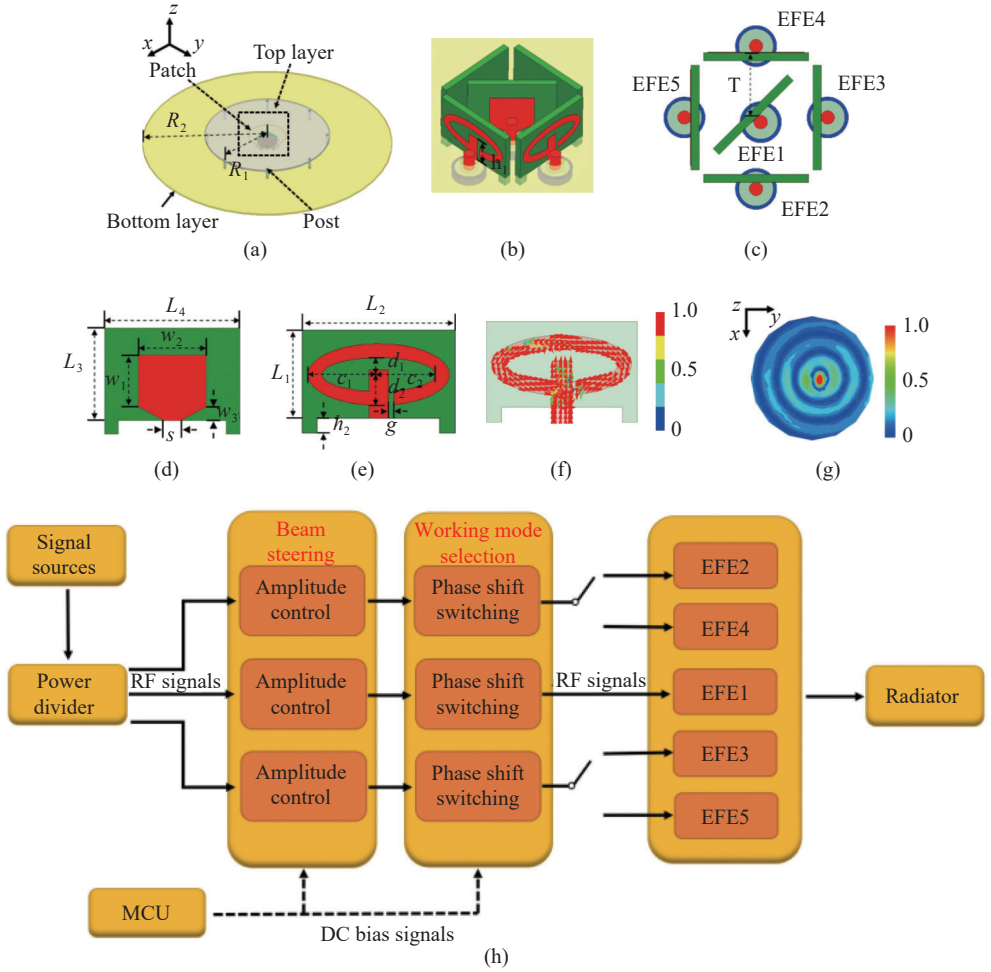

Figure 8 The configuration of the proposed azimuthal plane beam steering system. (a) The 3-D view of the overall system; (b) The 3-D view of the five EFEs; (c) The top view of the five EFEs; (d) The structure of EFE1; (e) The structure of EFE2 – EFE5; (f) The radiated electric field distribution of EFE3 in the *xoy* plane; (g) The current distribution of EFE3; (h) Scheme of the beam steering system.

with a relative dielectric constant $\varepsilon_r = 3.66$, loss tangent tan $\delta = 0.004$ and thickness of 0.762 mm. The optimized construction parameters shown in Figure 8 are listed in Table 2.

Table 2 Physical dimension of the azimuthal beam steering system (unit: mm)

R_1	R_2	h_1	h_2	L_1	L_2	L_3	L_4	c_1
50	180	3.1	1	5.7	10	6.8	10	4.6
d_1	c_2	d_2	W_1	W_2	W_3	s	g	T
2	3.99	1.1	3.8	5	1	1.27	0.365	3.18

To realize the desired amplitudes and phases at the feeding ports, the RF front-end circuit with the scheme shown in Figure 8(h) is designed. The RF signal is first divided by a one-to-three power divider, and then the signals' amplitudes are tuned, and their phase shifts selected. Finally, by employing two switches, they are fed into the desired feeding elements. For convenient regulation, all states of the amplitude-phase controlling circuits are digitally manipulated by a microprogrammed control unit (MCU). Note that the phase switching components in this design are only employed to switch the unidirectional and directional working modes of the system, while the beam steering functionality is achieved only by the amplitude controlling components. In this system, only two states of the phase shifts are required for the working mode switching, which can be achieved by one low-cost switch and two delay lines. This is distinct from the high-cost phased array, where numerous phase shift statuses are required to realize beam steering.

A prototype of the azimuthal beam steering system was fabricated, assembled, and measured. The radiator and feeding elements are shown in Figure 9(a). First, the reflection coefficients of each EFE were measured separately by using an Agilent Technologies E5071C network analyzer. The simulated and measured reflection coefficients of each EFE as functions of the source frequency are shown in Figure 10. The simulation results agree very well with the measured results. The overlapped −10 dB bandwidth ranges from 9.5 to 10.3 GHz. At the resonant frequency, i.e., ~10 GHz, the reflection coefficients of all feeding elements are below −14.6 dB. Because the reflection coefficients are small, the relationship of feeding powers between the central EFE and two selected surrounding EFEs, i.e., (13) can be approximately simplified as

$$P_{E1} = P_{Ei} + P_{Ej} \tag{14}$$

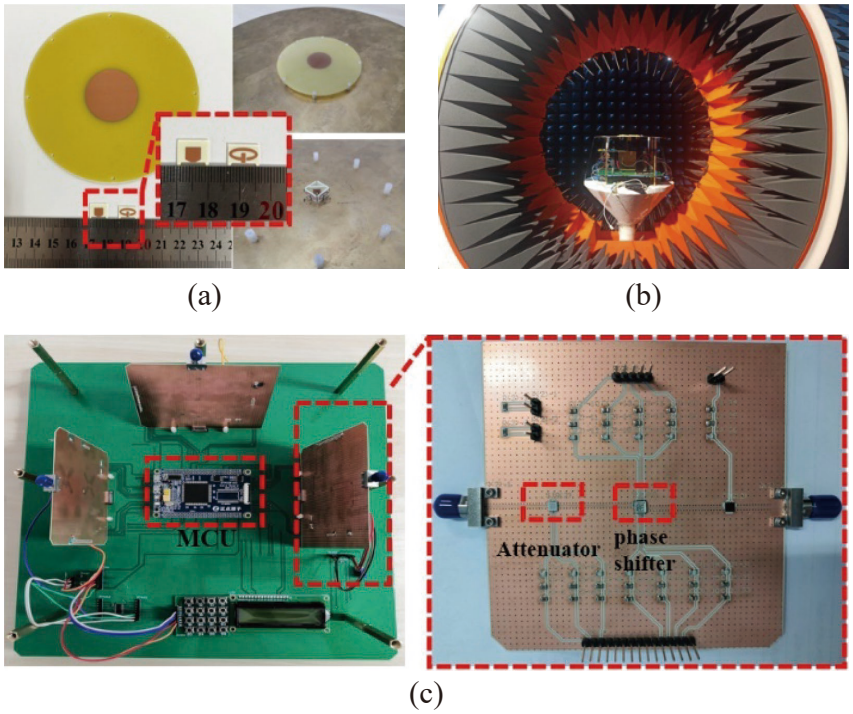

Figure 9 Fabricated azimuthal beam steering system. (a) 3-D isometric view before and after assembly; (b) Antenna under test (AUT) in the anechoic chamber; (c) Fabricated RF frontend circuits.

where i & j = 2 to 4 indicate the ith and jth EFE. Based on the above measurement results and previous theoretical analysis, we first configured the ideal amplitudes and phases of the feeding elements in the simulation to obtain the optimum beam steering performance to provide a configuration reference for the RF front-end circuit. The combinations of different amplitudes of feeding elements are listed in Table 3 and indicated as "ideal", and the corresponding

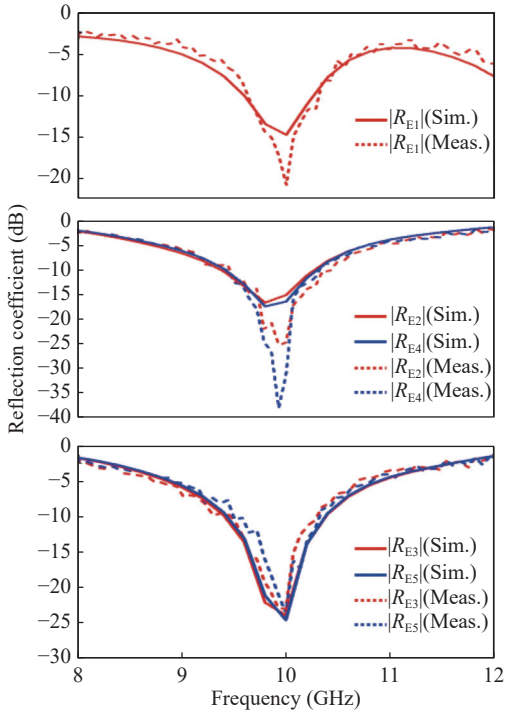

Figure 10 Simulated and reflection coefficients of the five EFEs.

radiation patterns under unidirectional and bidirectional modes are shown in Figure 11, which are indicated as "ideal simulation".

The fabricated RF frontend circuits are shown in Figure 9(c). According to the requirements listed in Table 3, we adjusted the utilized TGP2109-SM tunable phase shifter and CMD282C3 tunable attenuator to provide the closest phases and amplitudes in the three subcircuits. These chips are controlled by the STM32F103 MCU, and the scanning angle and working mode can be switched by the matrix keyboard. Note that the practical phases realized by the phase shifter are different from the ideal phase, but the phase difference between the elements is configured as close as possible to the ideal phase. We emphasize that the employment of phase shifters is only for the purpose of working mode switching. All the phases are fixed in each working mode, and they have no contribution to beam steering.

The practical amplitude combinations are shown in Table 3, and their corresponding simulation and measured radiation patterns when we look the 3-D patterns toward the $-z$ direction at 10.3 GHz are shown in Figure 11. A total of 7 unidirectional states and 3 bidirectional states, covering the whole azimuthal plane and scanning with a 45° incre-

Table 3 Combination of different amplitudes of feeding elements

Working mode	Case	—	EFE1	EFE2	EFE3	EFE4	EFE5	Peak realized gain (dBi)	Quadrants	ϕ
		—	P_{E1}	P_{E2}	P_{E3}	P_{E4}	P_{E5}			
Unidirectional mode	(a)	Ideal	2 W	0 W	1 W	1 W	0 W	8.28	2	135°
		Practical	1.77 W	0 W	1 W	1 W	0 W	Sim.: 8.15, Meas.: ~7.7		
	(b)	Ideal	2 W	0 W	0 W	1 W	1 W	Same with Case (a)	3	225°
		Practical	1.77 W	0 W	0 W	1 W	1 W			
	(c)	Ideal	2 W	1 W	0 W	0 W	1 W	Same with Case (a)	4	315°
		Practical	1.77 W	1 W	0 W	0 W	1 W			
	(d)	Ideal	2 W	1 W	1 W	0 W	0 W	Same with Case (a)	1	45°
		Practical	1.77 W	1 W	1 W	0 W	0 W			
	(e)	Ideal	1 W	1 W	0 W	0 W	0 W	6.71	1	0°
		Practical	1 W	1 W	0 W	0 W	0W	Sim.: 6.2, Meas.: ~5.4		
	(f)	Ideal	2 W	1 W	1W	0W	0W	Same with Case (a)	1	45°
		Practical	1.77 W	1 W	1W	0W	0W			
	(g)	Ideal	1 W	0 W	1W	0W	0W	Same with Case (e)	1	90°
		Practical	1 W	0 W	1W	0W	0W			
	The ideal fixed phase: for EFE1 is 70º, and for EFE2-4 is 0º The practical realized fixed phase: for EFE1 is 102º, and for EFE2-4 is ~56º									
Bidirectional mode	(h)	Ideal	1 W	1 W	0 W	0 W	0W	5.52	1&3	0°&180°
		Practical	1 W	1 W	0 W	0W	0W	Sim.: 5.28, Meas.: ~6.8		
	(i)	Ideal	2 W	1 W	1 W	0W	0W	4.49	1&3	45°&225°
		Practical	1.77 W	1 W	1 W	0W	0W	Sim.: 5.66, Meas.: ~6.1		
	(j)	Ideal	1 W	0 W	1W	0W	0W	Same with case (h)	1&3	90°&270°
		Practical	1 W	0 W	1W	0W	0W			
	The ideal fixed phase: for EFE1 is 210°, and for EFE2-4 is 0° The practical realized fixed phase: for EFE1 is −114°, and for EFE2-4 is ~56°									

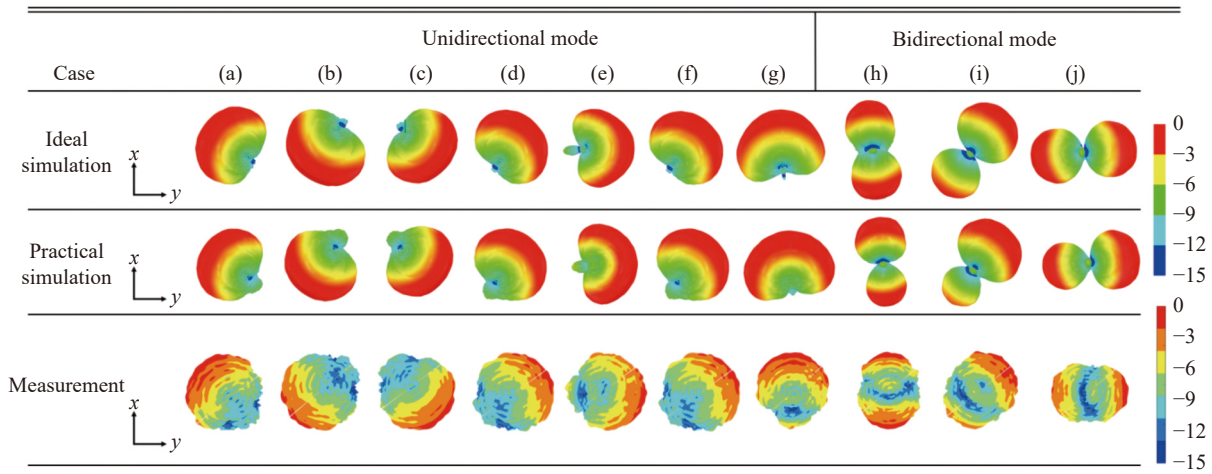

Figure 11 Simulated (with ideal and practical feeding amplitudes and phases) and measured radiation patterns of the proposed system operating under different unidirectional and bidirectional modes at 10.3 GHz. The cases correspond to those listed in Table 3.

mental angle in the first quadrant, are presented. In the measured results, it can be seen that due to the difference between the practical configurations and the ideal configurations, for the unidirectional mode, the front-to-back ratio decreases. For the bidirectional mode, the magnitude of the power radiated toward the two opposite directions would be unequal. From the comparison between the "Practical simulation" and "Measurement" in Figure 11, the measured results agree well with the simulated results, which verifies that the discrepancy in the radiation patterns indeed results from the error in the feeding configuration.

In addition to the normalized radiation patterns, the passive peak realized gain is calculated by considering the different input powers under different states and is shown in Table 3. The measured peak realized gains are smaller than the simulated ones in the different cases under the unidirectional mode, which is due to the additional loss in the prototype. However, they become larger than the simulated ones in the different cases under the bidirectional mode, which is mainly because the radiation magnitudes in the two opposite directions are not equal in the measurement, i.e., the radiation magnitude is enhanced in one direction but decreases in the other direction. Although there are discrepancies, the maximum difference in the peak realized gain in different cases is within 1.6 dB. Figure 12 further shows the E-plane cross-polarization and copolarization radiation patterns at 10.3 GHz under the unidirectional and bidirectional modes. The measured copolarized radiation in both working modes is at least 13 dB and 14 dB stronger than their cross-polarized counterparts, respectively. Due to fabrication, assembly and measurement errors, the pointing angle of the measured beam has a minor shift compared with the simulated beam.

Although the above measured radiation patterns are imperfect, the results can validate our proposed method for the azimuthal steering of power flow. In the future version of the system, to realize scanning angles with a higher resolution, the amplitudes controlling chips with larger bits (smaller amplitude step adjustment) should be utilized.

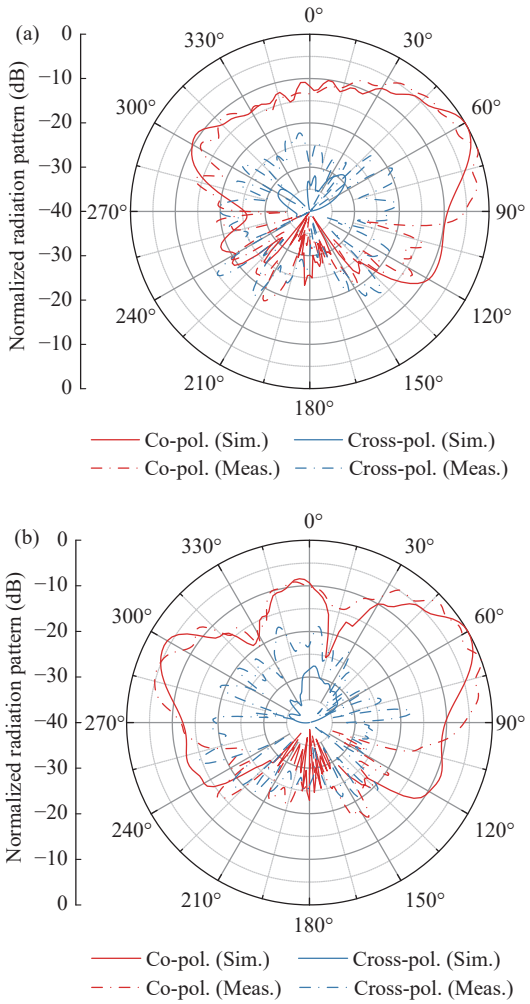

Figure 12 Cross-polarization and gain results of the proposed system operating under (a) unidirectional and (b) bidirectional modes at 10.3 GHz.

In addition, we also studied the frequency-dependent performance of this system. We take case (f) shown in Figure 11 as an example. The ideal and measured radiation pat-

terns at three frequency points (9.8, 10.2 and 10.6 GHz) within the −10 dB impedance matching frequency range are shown in Figure 13. It can be seen that with increasing frequency, the radiation patterns of the system configured with ideal feeding amplitudes and phases demonstrate good consistency, while the measured ones have larger variations in the front-to-back ratio. Again, the system is configured with practical amplitudes and phases, and the simulation results shown in Figure 13 agree well with the measured results, i.e., we can observe similar deterioration of the front-to-back ratio at lower frequencies. This comparison indicates that the reconfigurable source itself has a good frequency-independent performance within its impedance matching frequency range. However, the frequency-dependent characteristic of the feeding circuit would worsen its performance.

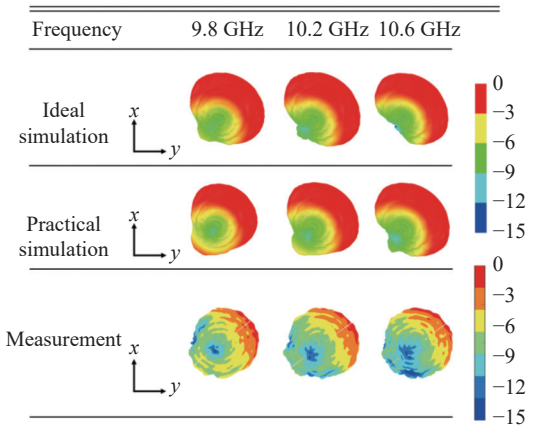

Figure 13 The (a) ideal simulation, (b) practical simulation and (c) measured radiation patterns of the proposed system operating at 9.8, 10.2 and 10.6 GHz.

From the above results and discussion, the azimuthal beam steering system can be well realized by applying our proposed reconfigurable source. Its two working modes can introduce unidirectional and bidirectional beam steering performance, which will have many potential applications in multiobject communication, tracking and monitoring scenarios. Here, we also demonstrate that the radiator in this system can be replaced by other antennas, lenses, and circuits, thus extending the application of the proposed reconfigurable source to many other advanced wireless transceivers and multifunctional circuits.

IV. Conclusion

A reconfigurable quintuple source that can arbitrarily regulate power flow by the amplitude-only synthesis method in the entire azimuthal plane was developed in this paper. Its working mechanism and two working modes, i.e., unidirectional and bidirectional modes, were analytically analyzed and validated. Then, practical structures of the source were designed in the PPW scenario and finally practically integrated in an azimuthal beam steering system. The prototype of the system was experimentally realized and measured, and good consistency of the S-parameters, working modes and beam steering performance was obtained between the measurement and simulation. This new technique paves the way for simple, compact, low-cost approaches for azimuthal beam steering systems.

Acknowledgement

This work was supported in part by the National Natural Science Foundation of China (Grant Nos. 62001065, 620 31006, 62071424, and 62027805), the Chongqing Natural Science Foundation (Grant Nos. cstc2021jcyj-msxmX0797 and cstc2019jcyjjqX0004), and the Zhejiang Provincial Natural Science Foundation of China (ZPNSFC) (Grant No. LD21F010002).

References

[1] L. Y. Ji, P. Y. Qin, Y. J. Guo, *et al*., "A wideband polarization reconfigurable antenna with partially reflective surface," *IEEE Transactions on Antennas and Propagation*, vol. 64, no. 10, pp. 4534–4538, 2016.

[2] W. Lin and H. Wong, "Wideband circular-polarization reconfigurable antenna with L-shaped feeding probes," *IEEE Antennas and Wireless Propagation Letters*, vol. 16, pp. 2114–2117, 2017.

[3] H. C. Sun and S. Sun, "A novel reconfigurable feeding network for quad-polarization-agile antenna design," *IEEE Transactions on Antennas and Propagation*, vol. 64, no. 1, pp. 311–316, 2016.

[4] M. R. LeRoy, S. Raman, M. Chu, *et al*., "High-speed reconfigurable circuits for multirate systems in SiGe HBT technology," *Proceedings of the IEEE*, vol. 103, no. 7, pp. 1181–1196, 2015.

[5] J. Xu, H. Wan, and Z. Y. Chen, "Sharp skirt bandpass filter-integrated single-pole double-throw switch with absorptive OFF-state," *IEEE Transactions on Microwave Theory and Techniques*, vol. 67, no. 2, pp. 704–711, 2019.

[6] J. Xu, F. Liu, and Z. Y. Feng, "Single-/dual-band bandpass filter-integrated single-pole double-throw switch using distributed coupling tri-mode resonators," *IEEE Transactions on Microwave Theory and Techniques*, vol. 68, no. 2, pp. 741–749, 2020.

[7] M. C. Tang, B. Y. Zhou, and R. W. Ziolkowski, "Low-profile, electrically small, Huygens source antenna with pattern-reconfigurability that covers the entire azimuthal plane," *IEEE Transactions on Antennas and Propagation*, vol. 65, no. 3, pp. 1063–1072, 2017.

[8] Z. T. Wu, M. C. Tang, M. Li, *et al*., "Ultralow-profile, electrically small, pattern-reconfigurable metamaterial-inspired Huygens dipole antenna," *IEEE Transactions on Antennas and Propagation*, vol. 68, no. 3, pp. 1238–1248, 2020.

[9] C. Kittiyanpunya and M. Krairiksh, "A four-beam pattern reconfigurable Yagi-Uda antenna," *IEEE Transactions on Antennas and Propagation*, vol. 61, no. 12, pp. 6210–6214, 2013.

[10] Y. J. Zhang, S. W. Tang, Z. X. Han, *et al*., "A low-profile microstrip vertically polarized endfire antenna with 360° beam-scanning and high beam-shaping capability," *IEEE Transactions on Antennas and Propagation*, vol. 70, no. 9, pp. 7691–7702, 2022.

[11] J. X. Li, Y. Y. Yuan, Y. X. Wang, *et al*., "Generating Bessel beams efficiently in microwave with high transmission metasurfaces," *IEEE Transactions on Magnetics*, vol. 57, no. 6, pp. 1–5, 2021.

[12] H. F. Huang and J. Zhang, "High-efficiency multifunction metasurface based on polarization sensitivity," *IEEE Antennas and Wireless Propagation Letters*, vol. 20, no. 8, pp. 1508–1512, 2021.

[13] C. L. Holloway, E. F. Kuester, J. A. Gordon, *et al*., "An overview of the theory and applications of metasurfaces: The two-dimensional equivalents of metamaterials," *IEEE Antennas and Propagation Magazine*, vol. 54, no. 2, pp. 10–35, 2012.

[14] X. Wan, T. Y. Chen, X. Q. Chen, *et al*., "Beam forming of leaky waves at fixed frequency using binary programmable metasurface," *IEEE Transactions on Antennas and Propagation*, vol. 66, no. 9, pp. 4942–4947, 2018.

[15] L. Zhang, Z. X. Wang, R. W. Shao, *et al*., "Dynamically realizing arbitrary multi-bit programmable phases using a 2-bit time-domain coding metasurface," *IEEE Transactions on Antennas and Propagation*, vol. 68, no. 4, pp. 2984–2992, 2020.

[16] J. Y. Dai, W. K. Tang, L. X. Yang, *et al*., "Realization of multi-modulation schemes for wireless communication by time-domain digital coding metasurface," *IEEE Transactions on Antennas and Propagation*, vol. 68, no. 3, pp. 1618–1627, 2020.

[17] X. Y. Luo, W. L. Guo, K. Chen, *et al*., "Active cylindrical metasurface with spatial reconfigurability for tunable backward scattering reduction," *IEEE Transactions on Antennas and Propagation*, vol. 69, no. 6, pp. 3332–3340, 2021.

[18] T. Haimov, K. Aydin, and J. Scheuer, "Reconfigurable holograms using VO_2-based tunable metasurface," *IEEE Journal of Selected Topics in Quantum Electronics*, vol. 27, no. 1, pp. 1–8, 2021.

[19] W. J. Chen, R. Chen, Y. Zhou, *et al*., "A switchable metasurface between meta-lens and absorber," *IEEE Photonics Technology Letters*, vol. 31, no. 14, pp. 1187–1190, 2019.

[20] G. Isić, D. C. Zografopoulos, D. B. Stojanović, *et al*., "Beam steering efficiency in resonant reflective metasurfaces," *IEEE Journal of Selected Topics in Quantum Electronics*, vol. 27, no. 1, pp. 1–8, 2021.

[21] B. B. Xing, Z. G. Liu, W. B. Lu, *et al*., "Wideband microwave absorber with dynamically tunable absorption based on graphene and random metasurface," *IEEE Antennas and Wireless Propagation Letters*, vol. 18, no. 12, pp. 2602–2606, 2019.

[22] H. B. Sedeh, M. M. Salary, and H. Mosallaei, "Active multiple access secure communication enabled by graphene-based time-modulated metasurfaces," *IEEE Transactions on Antennas and Propagation*, vol. 70, no. 1, pp. 664–679, 2022.

[23] R. J. Mailloux, *Phased Array Antenna Handbook*, 2nd ed. , Artech House, Boston, MA, USA, 2005.

[24] A. Puglielli, A. Townley, G. LaCaille, *et al*., "Design of energy- and cost-efficient massive MIMO arrays," *Proceedings of the IEEE*, vol. 104, no. 3, pp. 586–606, 2016.

[25] Y. Y. Bai, S. Q. Xiao, M. C. Tang, *et al*., "Wide-angle scanning phased array with pattern reconfigurable elements," *IEEE Transactions on Antennas and Propagation*, vol. 59, no. 11, pp. 4071–4076, 2011.

[26] M. C. Tang and R. W. Ziolkowski, "Multifunctional Huygens dipole antennas," in *Proceedings of the 13th European Conference on Antennas and Propagation*, Krakow, Poland, pp.1–3, 2019.

[27] M. C. Tang, T. Shi, and R. W. Ziolkowski, "A study of 28 GHz, planar, multilayered, electrically small, broadside radiating, Huygens source antennas," *IEEE Transactions on Antennas and Propagation*, vol. 65, no. 12, pp. 6345–6354, 2017.

[28] M. C. Tang, Z. T. Wu, T. Shi, *et al*., "Dual-band, linearly polarized, electrically small Huygens dipole antennas," *IEEE Transactions on Antennas and Propagation*, vol. 67, no. 1, pp. 37–47, 2019.

[29] M. C. Tang, X. M. Chen, T. Shi, *et al*., "A compact, low-profile, broadside radiating two-element Huygens dipole array facilitated by a custom-designed decoupling element," *IEEE Transactions on Antennas and Propagation*, vol. 69, no. 8, pp. 4546–4557, 2021.

[30] Z. T. Wu, M. C. Tang, T. Shi, *et al*., "Two-port, dual-circularly polarized, low-profile broadside-radiating electrically small Huygens dipole antenna," *IEEE Transactions on Antennas and Propagation*, vol. 69, no. 1, pp. 514–519, 2021.

[31] D. Yi, X. C. Wei, M. C. Tang, *et al*., "Regulating the direction that power flows in microwave transmission line systems with Huygens sources," *IEEE Transactions on Antennas and Propagation*, vol. 69, no. 1, pp. 594–599, 2021.

[32] F. J. Rodríguez-Fortuño, G. Marino, P. Ginzburg, *et al*., "Near-field interference for the unidirectional excitation of electromagnetic guided modes," *Science*, vol. 340, no. 6130, pp. 328–330, 2013.

[33] T. Van Mechelen and Z. Jacob, "Universal spin-momentum locking of evanescent waves," *Optica*, vol. 3, no. 2, pp. 118–126, 2016.

[34] L. Marrucci, "Spin gives direction," *Nature Physics*, vol. 11, no. 1, pp. 9–10, 2015.

[35] M. F. Picardi, A. V. Zayats, and F. J. Rodríguez-Fortuño, "Janus and Huygens dipoles: Near-field directionality beyond spin-momentum locking," *Physical Review Letters*, vol. 120, no. 11, article no. 117402, 2018.

[36] M. F. Picardi, A. V. Zayats, and F. J. Rodríguez-Fortuño, "Amplitude and phase control of guided modes excitation from a single dipole source: Engineering far- and near-field directionality," *Laser & Photonics Reviews*, vol. 13, no. 12, article no. 1900250, 2019.

[37] M. F. Picardi, M. Neugebauer, J. S. Eismann, *et al*., "Experimental demonstration of linear and spinning Janus dipoles for polarisation- and wavelength-selective near-field coupling," *Light:Science & Applications*, vol. 8, article no. 52, 2019.

[38] A. M. H. Wong and G. V. Eleftheriades, "Active Huygens' box: Arbitrary electromagnetic wave generation with an electronically controlled metasurface," *IEEE Transactions on Antennas and Propagation*, vol. 69, no. 3, pp. 1455–1468, 2021.

[39] G. X. Zhu, K. B. Huang, V. K. N. Lau, *et al*., "Hybrid beamforming via the kronecker decomposition for the millimeter-wave massive MIMO systems," *IEEE Journal on Selected Areas in Communications*, vol. 35, no. 9, pp. 2097–2114, 2017.

[40] W. Roh, J. Y. Seol, J. Park, *et al*., "Millimeter-wave beamforming as an enabling technology for 5G cellular communications: Theoretical feasibility and prototype results," *IEEE Communications Magazine*, vol. 52, no. 2, pp. 106–113, 2014.

[41] M. Jafri, A. Anand, S. Srivastava, *et al*., "Robust distributed hybrid beamforming in coordinated multi-user multi-cell mmWave MIMO systems relying on imperfect CSI," *IEEE Transactions on Communications*, vol. 70, no. 12, pp. 8123–8137, 2022.

[42] S. Sun, T. S. Rappaport, R. W. Heath, *et al*., "MIMO for millimeter-wave wireless communications: Beamforming, spatial multiplexing, or both?," *IEEE Communications Magazine*, vol. 52, no. 12, pp. 110–121, 2014.

[43] C. A. Balanis, *Antenna Theory*: *Analysis and Design*, 3rd ed., John Wiley & Sons, New York, NY, USA, 2005.

[44] J. D. Kraus and R. J. Marhefka, *Antennas*: *For All Applications*, 3rd ed. , McGraw-Hill, New York, NY, USA, 2001.

[45] H. Yagi, "Beam transmission of ultra short waves," *Proceedings of the IEEE*, vol. 85, no. 11, pp. 1864–1874, 1997.

Da Yi received the B.S. and Ph.D. degrees in electronic science and technology from Zhejiang University, Hangzhou, China, in 2014 and 2019, respectively. He currently works in Chongqing University, Chongqing, China as a Tenure-track Assistant Professor.

Dr. Yi is the recipient of the awards in 8 international conferences. His current research interests include the design of small antenna arrays and high-speed circuits.

Zhiyang Qi received the B.S. degree in communication engineering in the School of Physics and Electronic-electrical Engineering, Qufu Normal University, China, in 2019. He is currently pursuing the postgraduate degree in the School of Microelectronics and Communication Engineering, Chongqing University, China. His research interests include coupling suppression and utilization in antenna arrays and high-speed circuits.

Mingchun Tang received the B.S. degree in physics from the Neijiang Normal University, Neijiang, China, in 2005 and the Ph.D. degree in Radio Physics from the University of Electronic Science and Technology of China (UESTC), in 2013. From August 2011 to August 2012, he was also with the Department of Electrical and Computer Engineering, The University of Arizona, Tucson, AZ, USA, as a Visiting Scholar. He is currently a Full Professor in the School of Microelectronics and Communication Engineering, Chongqing University, China. His research interests include electrically small antennas, RF circuits, metamaterial designs and their applications. Prof. Tang is the founding Chair of the IEEE AP-S / MTT-S Joint Chongqing Chapter.
(Email: tangmingchun@cqu.edu.cn)

Dajiang Li was born in Jiangxi Province, China. He received the B.S. degree in electronic information science and technology from the Chongqing Normal University, Chongqing, China, in 2017, and the Ph.D. degree in electric circuit and system from the Chongqing University, Chongqing, in 2023. In 2023, he joined the Chongqing University of Posts and Telecommunications, Chongqing, where he is currently a Lecturer. His current research interests include filtennas, multi-functional antennas, and microwave circuits.

Yilin Lang received the B.S. degree in communication engineering from Chongqing University, Chongqing, China, in 2021, where he is currently pursuing the Ph.D. degree in information and communication engineering at the School of Microelectronics and Communication Engineering, Chongqing University, Chongqing, China. His current research interests include filtering antenna, antenna array and their applications.

Xingchang Wei received the Ph.D. degree in electrical engineering from Xidian University, Xi'an, China, in 2001. From 2001 to 2010, he was with the A-STAR Institute of High-Performance Computing, Singapore, as a Research Fellow, Senior Research Engineer, and Research Scientist. In 2010, he joined Zhejiang University, China, as a Full Professor. He has authored one book, co-authored one book chapter, and more than 130 papers published in IEEE Transactions and international conferences. His main research interests include electromagnetic interference modeling and testing, power and signal integrities design. He is the recipient of the Singapore Institution of Engineers Prestigious Engineering Achievement Award in 2007, for his contribution to the development of the reverberation chamber for the electromagnetic compatibility measurement, New Century Professional Award from China Ministry of Education, and numerous paper awards from IEEE international conferences.